INTERNATIONAL JOURNAL FOR NUMERICAL METHODS IN FLUIDS, VOL. 25, 697–717 (1997)

A STAGGERED CONTROL VOLUME SCHEME FOR UNSTRUCTURED TRIANGULAR GRIDS

S. RIDA, F. McKENTY, F. L. MENG AND M. REGGIO*

Department of Mechanical Engineering, École Polytechnique de Montréal, CP 6079, Succ. Centre-ville,
Montréal, Québec H3C 3A7, Canada

SUMMARY

The purpose of this work is to introduce and validate a new staggered control volume method for the simulation of 2D/axisymmetric incompressible flows.

The present study introduces a numerical procedure for solving the Navier–Stokes equations using the primitive variable formulation. The proposed method is an extension of the staggered grid methodology to unstructured triangular meshes for a control volume approach which features ease of handling of irregularly shaped domains. Two alternative elements are studied: transported scalars are stored either at the sides of an element or at its vertices, while the pressure is always stored at the centre of an element. Two interpolation functions were investigated for the integration of the momentum equations: a skewed mass-weighted upwind function and a flow-oriented exponential shape function. The momentum equations are solved over the covolume of a side or of a vertex and the pressure–velocity coupling makes use of a localized linear reconstruction of the discontinuous pressure field surrounding an element in order to obtain the pressure gradient terms. The pressure equation is obtained through a discretization of the continuity equation which uses the triangular element itself as the control volume.

The method is applied to the simulation of the following test cases: backward-facing step flow, flow over a two-dimensional obstacle and flow in a pipe with sudden contraction of cross-sectional area. All numerical investigations are compared with experimental data from the literature. A grid convergence and error analysis study is also carried out for flow in a driven cavity.

Results compared favourably with experimental data and so the new control volume scheme is deemed well suited for the prediction of incompressible flows in complex geometries. © 1997 John Wiley & Sons, Ltd.

Int. J. Numer. Meth. Fluids, **25**: 697–717 (1997)

No. of Figures: 16. No. of Tables: 1. No. of References: 18.

KEY WORDS: control volume; staggered grid; unstructured mesh; incompressible flow

INTRODUCTION

The solution of the incompressible flow equations presents a particular difficulty which is related to the fact that none of the equations can be directly identified as governing the pressure. Using

---

* Correspondence to: M. Reggio, Department of Mechanical Engineering, École Polytechnique de Montreal, CP 6079, Succ. Centre-Ville, Montréal, Québec H3C 3A7, Canada

Contract grant sponsor: National Sciences and Engineering Research Council of Canada (NSERC)
Contract grant sponsor: FCAR
Contract grant sponsor: Centre des Technologies due Gaz Nautrel (CTGN)

CCC 0271–2091/97/060697–21 $17.50

Received 5 June 1995
Revised 20 November 1996

algorithms based upon artificial compressibility,[1] or taking the limit of the compressible flow equations through preconditioning[2] to regularize the eigenvalues, succeeds in providing a link between the equations. These techniques are required to overcome the pressure oscillatory patterns which result from the singular coefficient matrices. Furthermore, if the artificial compressibility approach can successfully predict unsteady flows using implicit schemes, it is not time-accurate for explicit time-marching procedures.[3] Another approach commonly used to alleviate this difficulty is a staggered arrangement of the variables. Initially introduced by Harlow and Welch[4] on Cartesian grids, it has led to several variations depending on the location of the variables. These variations have been extensively studied and compared with equivalent collocated schemes by Shih *et al.*[5] The staggered arrangement is equivalent to the unequal-order interpolation for pressure and velocity that is used to achieve stability in the finite-element context as expressed by the Ladyzhenskaya–Babuska–Brezzi condition.

The application of such schemes to irregular geometries of practical interest has led to the necessity of extending these to curvilinear meshes. Contravariant and/or Cartesian velocity components have been considered, while the pressure, as in the Cartesian case, may be considered to be piecewise constant or piecewise linear, the first alternative being the most popular. A curvilinear co-ordinate system naturally generates a logical data stucture which preserves the basic arrangement of the variables of structured Cartesian grids. However, not all arrangements extend readily to curvilinear grids and many authors have found it convenient to revert to collocated schemes to avoid the overhead resulting from the data structure of staggered schemes.[6] In both cases, collocated and staggered, the problem of devising an effective velocity–pressure coupling to yield a divergence-free velocity field remains.

Adequate and cost-effective treatment of complex geometries with additional requirements such as adaptivity leads inevitably to the use of unstructured grids. Once this point has been reached, the advantages of using quadrilaterals (in 2D) as the basic discretization elements are no longer obvious and other polygonal shapes may be adopted. However, the basic issue of the velocity–pressure coupling still remains for unstructured grids and several successful attempts have been reported[7] using a collocated arrangement of the variables. These essentially rely on averaging techniques for the coefficients of the momentum equations at the cell interfaces, since the velocity is not available at the faces because of the non-staggered arrangement. In fact, the evaluation and storage of both nodal and interface velocities are then required. Hence the choice of collocation may be questioned. Along these lines the covolume approach using a Voronoi–Delaunay mesh has been introduced by Nicolaides[8] as the first attempt at a staggered discretization for unstructured grids.

The present investigation proposes a distinct avenue to extend the staggered grid methodology to unstructured grids using a general triangulation as the primal mesh. In keeping with the staggered grid approach, separate locations and control volumes are used for different variables. However, unlike the covolume approach of Nicolaides, the same control volume is used for both velocity components, because no orthogonality properties are imposed on the mesh. The main difficulties encountered in this approach are the handling of the pressure gradient and the discretization of the convective term. The contribution of the pressure gradients to the momentum equations cannot be obtained by integration of the pressure along the boundary of the velocity control volume but must be determined via a reconstruction of the pressure field dictated by the special configuration of the unstructured staggered grid. For this purpose, several reconstruction schemes have been investigated. As for the discretization of the convective term, two interpolation functions were studied for the integration of the scalar transport equation: the skewed mass-weighted upwind function proposed by Schneider and Raw[9] and the flow-oriented exponential shape function first introduced by Baliga and Patankar.[10] However, the flow-oriented exponential shape function yielded unsatisfactory results for swirling flows and so only the skewed mass-weighted upwind function was retained.

GOVERNING EQUATIONS

The equations governing the mass, momentum and transport of scalar quantities for unsteady two-dimensional plane or axisymmetric incompressible flows are written as

$$\nabla \cdot (\rho \vec{v}) = 0, \tag{1}$$

$$\frac{\partial}{\partial t}(\rho \vec{v}) + \nabla \cdot [\rho \vec{v} \otimes \vec{v} - \mu(\nabla \vec{v} + \nabla^{\mathrm{T}} \vec{v})] + \nabla \cdot (P\tilde{\mathbf{G}}) - \vec{S} = \vec{0}, \tag{2}$$

$$\frac{\partial}{\partial t}(\rho \phi) + \nabla \cdot (\rho \vec{v} \phi - \Gamma_{\phi} \nabla \phi) - S_{\phi} = 0, \tag{3}$$

where $\otimes$ is the tensor product operator, $\tilde{\mathbf{G}}$ is the metric tensor and Γ_{ϕ} is the diffusion coefficient of the dependent variable ϕ. Integrating equations (1)–(3) over a given covolume Ω_{c} and using the Gauss theorem yields the following integral forms of the governing equations.

Continuity equation

$$\oint_{\partial \Omega_{\mathrm{c}}} (\rho \vec{v}) \cdot \vec{n} r \, \mathrm{d}l = 0. \tag{4}$$

Momentum equations

The first step is to transfer the vector form of the conservation of momentum into transport equations for scalar variables (u, v). This is achieved by projecting equation (2) in the appropriate basis. Hence multiplying equation (2) by a vector $\vec{g}$ ($\vec{g} = \vec{e}_x$ or $\vec{g} = \vec{e}_y$) yields

$$\frac{\partial}{\partial t}(\rho v_g) + \nabla \cdot (\rho \vec{v} v_g - \mu \nabla v_g) + (\rho \vec{v} \otimes \vec{v} - \mu \nabla \vec{v}) : \nabla \vec{g} + \nabla \cdot (P \vec{g}) + (PI) \nabla \vec{g} = 0, \tag{5}$$

where $v_g = \vec{v} \cdot \vec{g}$ and the symbol ‘ : ’ represents the double contraction operator. Then integrating equation (5) over the covolume Ω_{c} and using the Gauss theorem yields

$$\int_{\Omega_{\mathrm{c}}} \frac{\partial}{\partial t}(\rho v_g) \, \mathrm{d}V + \oint_{\partial \Omega_{\mathrm{c}}} (\rho \vec{v} v_g - \mu \nabla v_g) \cdot \vec{n} \, \mathrm{d}s + \int_{\Omega_{\mathrm{c}}} (\rho \vec{v} \otimes \vec{v} - \mu \nabla \vec{v}) : \nabla \vec{g} \, \mathrm{d}V$$
$$+ \oint_{\partial \Omega_{\mathrm{c}}} P \vec{g} \cdot \vec{n} \, \mathrm{d}s + \int_{\Omega_{\mathrm{c}}} (P\tilde{\mathbf{G}}) : \nabla \vec{g} \, \mathrm{d}V = 0. \tag{6}$$

For the u-momentum equation, $\vec{g}$ in (6) is replaced by $\vec{e}_x$, and since the unit vector $\vec{e}_x$ is constant, $\nabla \vec{e}_x = \tilde{\mathbf{0}}$; thus the equation reduces to

$$\int_{\Omega_{\mathrm{c}}} \frac{\partial}{\partial t}(\rho u) r \, \mathrm{d}A + \oint_{\partial \Omega_{\mathrm{c}}} (\rho \vec{v} u - \mu \nabla u) \cdot \vec{n} r \, \mathrm{d}l + \oint_{\partial \Omega_{\mathrm{c}}} P \vec{e}_x \cdot \vec{n} r \, \mathrm{d}l = 0. \tag{7}$$

Similarly, for the v-momentum equation, $\vec{v}$ is replaced by $\vec{e}_y$ in Cartesian co-ordinates or $\vec{e}_r$ in cylindrical co-ordinates. Since $\vec{e}_r$ is not a constant vector, it follows that $\nabla \vec{e}_r \neq \tilde{\mathbf{0}}$ and the following integral equation is obtained:

$$\int_{\Omega_{\mathrm{c}}} \frac{\partial}{\partial t}(\rho v) r \, \mathrm{d}A + \oint_{\partial \Omega_{\mathrm{c}}} (\rho \vec{v} v - \mu \nabla v) \cdot \vec{n} r \, \mathrm{d}l + \int_{\Omega_{\mathrm{c}}} 2\mu \frac{v}{r^2} \alpha_{\mathrm{axi}} r \, \mathrm{d}A$$
$$+ \oint_{\partial \Omega_{\mathrm{c}}} P \vec{e}_y \cdot \vec{n} r \, \mathrm{d}l - \int_{\Omega_{\mathrm{c}}} \frac{P}{r} \alpha_{\mathrm{axi}} r \, \mathrm{d}A = 0. \tag{8}$$

Scalar ϕ transport equation

$$\int_{\Omega_c} \frac{\partial}{\partial t}(\rho\phi) r \, \mathrm{d}A + \oint_{\partial\Omega_c} (\rho\vec{v}\phi - \Gamma_\phi \nabla\phi) \cdot \vec{n} r \, \mathrm{d}l - \int_{\Omega_c} S_\phi r \, \mathrm{d}A = 0. \tag{9}$$

For Cartesian co-ordinates, $r = 1$, $\alpha_{\mathrm{axi}} = 0$, $\mathrm{d}v = z \, \mathrm{d}A$ and $\mathrm{d}s = z \, \mathrm{d}l$, whereas for cylindrical co-ordinates, $r = y$, $\alpha_{\mathrm{axi}} = 1$, $\mathrm{d}v = 2\pi r \, \mathrm{d}A$ and $\mathrm{d}s = 2\pi r \mathrm{d}l$.

NUMERICAL METHOD

The extension of the classical staggered scheme for Cartesian grids to unstructured meshes yields several possible configurations. Nicolaides[8] has proposed a set of covolumes which possess an orthogonality property derived from the Voronoi–Delaunay triangulation. In the present study the centroids instead of the circumcentres of the triangles are used to define the dual cells. This provides flexibility when adapting the grid. For this set of covolumes, two arrangements for the location of the variables have been investigated. These result in a staggered unequal-order scheme. In the first arrangement, shown in Figure 1(a), the pressure is stored at the centroid of the element and the velocities are stored at the midpoints of the sides (side-centred). The second variation (Figure 1(b)) has the velocities stored at the vertices of the element (vertex-centred) and the pressure at the centroid.[11] For the continuity equation, both configurations use the triangular element itself as the control volume, whereas the covolume for the momentum (shaded area in Figure 1) is a polygon centred on either a side of a vertex.

Discretization of transport equation

The conservation and transport of a scalar using these control volumes yield

$$\int_{iaoci} \frac{\partial}{\partial t}(\rho\phi) r \, \mathrm{d}A + \int_a^o \vec{J} \cdot \vec{n} r \, \mathrm{d}l + \int_o^c \vec{J} \cdot \vec{n} r \, \mathrm{d}l - \int_{iaoci} S_\phi r \, \mathrm{d}A \\ + (\text{similar contributions from other elements associated with node } i) = 0, \tag{10}$$

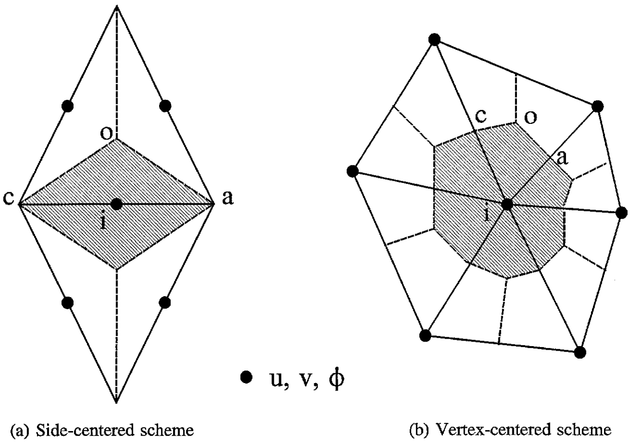

(a) Side-centered scheme (b) Vertex-centered scheme

Figure 1. Control volume for transported scalar

where

$$\vec{J} = \rho\vec{v}\phi - \Gamma_\phi \nabla\phi.$$

The discretization of the transient term using the forward Euler method yields

$$\int_{iaoci} \frac{\partial}{\partial t}(\rho\phi)\,\mathrm{d}V = A_i \bar{r}_{A_i}\rho \frac{\phi_i^{n+1} - \phi_i^n}{\Delta t}, \tag{11}$$

where A_i is the area of control volume *iaoci* and $\bar{r}_{A_i}$ is the radial co-ordinate of the centroid of area A_i in cylindrical co-ordinates (i.e. $r = \bar{r}_{A_i} = 1$ for Cartesian co-ordinates); ϕ_i^{n+1} and ϕ_i^n are the values of ϕ_i at time levels $n+1$ and n respectively and at variable location i.

The convection–diffusion flux $\vec{J}$ may be expressed in the basis $(\vec{e}_x, \vec{e}_y)$ as

$$\vec{J} = J_x \vec{e}_x + J_y \vec{e}_y, \tag{12}$$

where

$$J_x = \rho u\phi - \Gamma_\phi \frac{\partial\phi}{\partial x}, \qquad J_y = \rho v\phi - \Gamma_\phi \frac{\partial\phi}{\partial y}. \tag{13}$$

The integration of the convection–diffusion flux in equation (10) can then be approximated as

$$\int_a^o \vec{J}\cdot\vec{n}\,\mathrm{d}s = \int_a^o (J_x n_x + J_y n_y)\,\mathrm{d}s = [(J_x)_p(n_x)_p + (J_y)_p(n_y)_p]s_{ao}r_{ao}, \tag{14}$$

$$\int_o^c \vec{J}\cdot\vec{n}\,\mathrm{d}s = \int_o^c (J_x n_x + J_y n_y)\,\mathrm{d}s = -[(J_x)_t(n_x)_t + (J_y)_t(n_y)_t]s_{oc}r_{oc}, \tag{15}$$

where $(n_x)_p$, $(n_y)_p$ and $(n_x)_t$, $(n_y)_t$ are the components of the outward normal in the clockwise direction of integration faces $\overline{ao}$ and $\overline{oc}$ respectively and r is the radius at the midpoint of a face (Figure 2). The value of the dependent variable ϕ appearing in the convection flux is determined using an upwind interpolation function as described further; other properties such as the convecting velocity and the source term are assumed to vary linearly in the element.

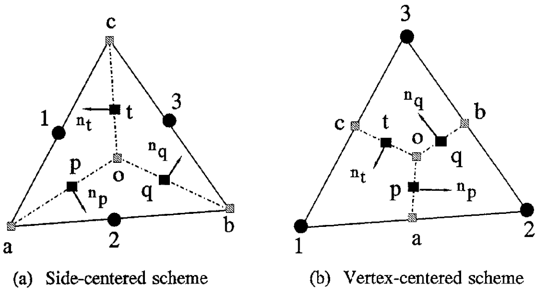

(a) Side-centered scheme (b) Vertex-centered scheme

● u, v, ϕ

■ Integration Points p, q and t

▨ Endpoints of sub-control volume a,b,c and o

Figure 2. Details of discretization and related nomenclature

Finally, summing the contributions of the transient, convection–diffusion and source terms together with the boundary condition for ϕ, the final form of the discretized transport equation can be cast in the usual way[12] as

$$a_i\phi_i^{n+1} + \sum a_{nb}\phi_{nb}^{n+1} = a_i^0\phi_i^n + d_i^\phi, \tag{16}$$

where the summation is over the neighbours (nb) surrounding a computational point i and $a_i^0 = A_i\bar{r}_{A_i}\rho/\Delta t$ as shown in (11). For the steady state formulation the contribution of the transient term is omitted and the discretized transport equation reduces to

$$a_i\phi_i + \sum a_{nb}\phi_{nb} = d_i^\phi. \tag{17}$$

One convenient characteristic of the side-centred scheme is that the number of neighbours is always four, whereas in the case of the vertex-centred scheme the number of neighbours depends on the mesh configuration. This helps to reduce the matrix bandwidth especially when judicious grid numbering is used.

Interpolation function

Both the side-centred and vertex-centred schemes originally made use of a hybrid interpolation function for the integration of the convection–diffusion flux.[11] This hybrid function combines the flow-oriented upwind function of Baliga and Patankar[10] and a variation of the skewed mass- weighted upwind function of Schneider and Raw.[9]

The flow-oriented upwind function for a dependent variable ϕ is the solution of the convection–diffusion equation without a source term. It may be expressed as

$$\phi = AZ + BY + C, \qquad Z = \frac{\Gamma_\phi}{\rho U_{\text{av}}}\left[\exp\left(\frac{\rho U_{\text{av}}}{\Gamma}(X - X_{\max})\right) - 1\right], \tag{18}$$

where U_{av} is the average velocity in an element and (X, Y) is a local co-ordinate system in which the X-direction is aligned with the average velocity. A, B and C are coefficients that can be determined uniquely in terms of the local (X, Y) co-ordinates of nodes 1, 2 and 3 and the corresponding values of ϕ.

The skewed mass-weighted upwind function of Schneider and Raw[9] for quadrilateral elements was extended to triangular elements of arbitrary aspect ratios by Rida.[11] Thus, by using the midpoint approximation, the value of ϕ at integration point p (Figure 2) is determined in the following way: if $\dot{m}_p > 0$, then

$$\phi_p = f\phi_t + (1 - f)\phi_1, \qquad f_p = \min\left[\max\left(\frac{\dot{m}_t}{\dot{m}_p}, 0\right), 1\right]; \tag{19}$$

if $\dot{m}_p < 0$, then

$$\phi_p = f\phi_q + (1 - f)\phi_2, \qquad f_p = \min\left[\max\left(\frac{\dot{m}_q}{\dot{m}_p}, 0\right), 1\right]. \tag{20}$$

Where $\dot{m}_p = [r\rho(\vec{v}\cdot\vec{n})]_p s_{ao}$ is the mass flow rate across integration face p, $\dot{m}_q$ and $\dot{m}_t$ are the mass flow rates across integration faces q and t respectively and s_{ao} is the length of face p. Combining the expressions of (19) and (20) together with similar expressions for integration faces q and t, the values ϕ_p, ϕ_q and ϕ_t at integration points p, q and t can be expressed as

$$\begin{aligned}\phi_p &= \zeta_p\phi_t + \varsigma_p\phi_1 + \sigma_p\phi_2 + \chi_p\phi_q,\\ \phi_q &= \zeta_q\phi_p + \varsigma_q\phi_2 + \sigma_q\phi_3 + \chi_q\phi_t,\\ \phi_t &= \zeta_t\phi_q + \varsigma_t\phi_3 + \sigma_t\phi_1 + \chi_t\phi_p.\end{aligned} \tag{21}$$

Simultaneous solutions for ϕ_p, ϕ_q and ϕ_t in terms of node values ϕ_1, ϕ_2 and ϕ_3 are determined from (21), where ζ_j, ς_j, σ_j and χ_j ($j=p$, q, t) are coefficients to which the following values are assigned:

$$\begin{aligned}\dot{m}_j > 0&: \quad \zeta_j = f_j, \quad \varsigma_j = 1 - f_j, \quad \sigma_j = 0, \quad \chi_j = 0,\\ \dot{m}_j < 0&: \quad \zeta_j = 0, \quad \varsigma_j = 0, \quad \sigma_j = 1 - f_j, \quad \chi_j = f_j.\end{aligned} \tag{22}$$

The values of ϕ_p, ϕ_q and ϕ_t are then used in the calculation of the fluxes at the integration faces.

The computation of the convective flux in a particular element was based on the local Peclet number of that element: when $Pe \leqslant Pe_{\max}$, the exponential function was used; when $Pe > Pe_{\max}$, the skewed mass-weighted upwind function was used. The Peclet number of an element is defined as

$$Pe = \frac{\rho U_{\mathrm{av}}}{\Gamma}(X_{\max} - X_i), \tag{23}$$

where X_i is the X-co-ordinate at variable locations. The values $Pe_{\max} = 10$ for laminar flow and $Pe_{\max} = 2$ for turbulent flow were found to give a good transition. The results obtained with the hybrid interpolation function were only marginally different from those obtained solely with the skewed mass-weighted upwind function.[11] Furthermore, for turbulent swirling flows[11] and turbulent reacting flows,[13] only the mass-weighted upwind scheme proved satisfactory. Accordingly, the skewed mass-weighted upwind function modified for triangular elements is the only one used in the present study.

The calculation of the diffusion terms is based on a linear interpolation function determined from the values of ϕ at points 1, 2 and 3 and their corresponding (x, y) locations (Figure 2).

Pressure–velocity coupling

In the process of discretizing the governing equations, the pressure–velocity coupling step must be undertaken when, in the overall solution procedure, the momentum equations are segregated from the continuity equation, which is the case in the present study.

The derivations of both the side-centred and vertex-centred schemes are essentially identical, except for details pertaining to the coupling of pressure and velocity since the momentum covolumes are different. Although both schemes yield results with comparable accuracy, it was found that the side-centred scheme converges more rapidly and that Neumann-type boundary conditions on solid walls are more easily implemented. The pressure-velocity coupling will therefore only be described for the side-centred scheme, as all computations presented in this paper were carried out solely with this scheme.

The pressure-velocity coupling relation is established by combining the momentum and continuity equations. Figure 3 shows the covolume used for the momentum equations in the calculation of point i, its neighbouring points $k = 1, 2, 3, 4$ and the integration points $j = 1, 2, 3, 4$. L and R represent the centroids of each triangular element having a common side i in this covolume. As the pressure is considered piecewise constant by element, the pressure integrals in the momentum equations (7) and (8) may be discretized as

$$\oint_{\partial\Omega_c} P\vec{e}_x \cdot \vec{n}r \, \mathrm{d}l \approx \sum_{j=1}^{4} P_j r_j s_j (\vec{n}_j \cdot \vec{e}_x) = \Delta P_i r_i s_i N_{ix}, \tag{24}$$

$$\oint_{\partial\Omega_c} P\vec{e}_y \cdot \vec{n}r \, \mathrm{d}l - \int_{\Omega_c} P\alpha_{\mathrm{axi}} \, \mathrm{d}A \approx \sum_{j=1}^{4} P_j r_j s_j (\vec{n}_j \cdot \vec{e}_y) - (P_R A_R + P_L A_L)\alpha_{\mathrm{axi}} = \Delta P_i r_i s_i N_{iy}, \tag{25}$$

where $\vec{N}_t$ is a normal directed from triangle L towards triangle R, as shown in Figure 3. Discretizing and casting in the form of (16), the discretized momentum equations are written as

$$\begin{aligned} a_i^u u_i^{n+1} + \sum_{k=1}^{4} a_k^u u_k^{n+1} &= a_i^0 u_i^n - \Delta P_i r_i s_i N_{ix} + d_i^u, \\ a_i^v v_i^{n+1} + \sum_{k=1}^{4} a_k^v v_k^{n+1} &= a_i^0 v_i^n - \Delta P_i r_i s_i N_{iy} + d_i^v. \end{aligned} \tag{26}$$

The control volume for the continuity equation is the triangular element itself shown by the full lines in Figure 4. Using the midpoint approximation for the velocity in (4) yields

$$\sum_{i=1}^{3} \rho r_i \vec{v}_i^{n+1} \cdot \vec{n}_i s_i = 0, \tag{27}$$

where s_i is the length of side i and $\vec{n}_i$ represents the outward normal of each integration side i of element P_0.

An algebraic equation for pressure is then derived by substituting the discrete momentum relation (26) into the discrete continuity relation (27). Using this procedure, the pressure equation is derived from the three pressure differences ΔP_i ($i = 1, 2, 3$) that drive the three normal velocities of an element. In fact, these pressure differences appear in the continuity equation when the components of the velocity vector $\vec{v}_i^{n+1}$ in (27) are replaced by the components u_i^{n+1} and v_i^{n+1} of the momentum equation (26). The pressure equation takes the form

$$c_0 P_0 + \sum_{i=1}^{3} c_i P_i = \xi, \tag{28}$$

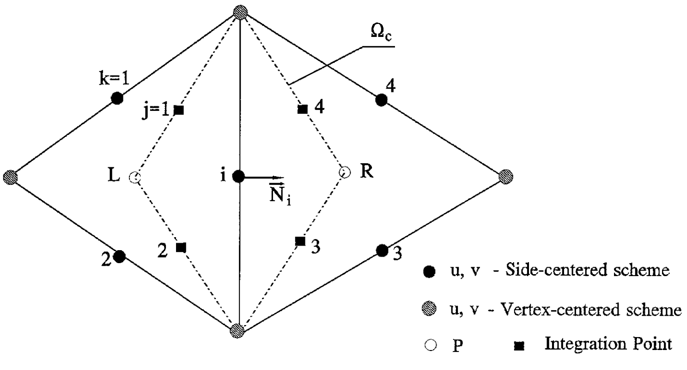

Figure 3. Covolume used for deriving pressure–velocity closure

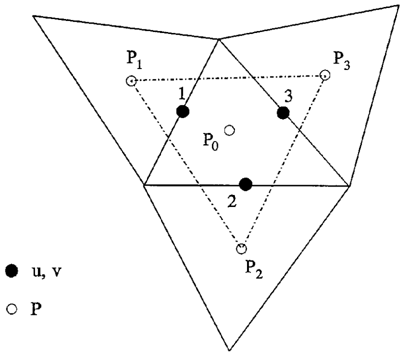

Figure 4. Node cluster involved in discretized pressure equation

with

$$c_i = \rho r_i^2 s_i^2 \left(\frac{n_{ix}^2}{a_i^u} + \frac{n_{iy}^2}{a_i^v} \right), \qquad c_0 = -\sum_{i=1}^{3} c_i, \qquad \xi = \sum_{i=1}^{3} \rho r_i s_i (\vec{v}_i^* \cdot \vec{n}_i),$$

where the components of vector $\vec{v}_i^*$ are defined as

$$u_i^* = \frac{-\sum_{k=1}^{4} a_k^u u_k^n + a_i^0 u_i^n + d_i^u}{a_i^u}, \qquad v_i^* = \frac{-\sum_{k=1}^{4} a_k^v v_k^n + a_i^0 v_i^n + d_i^v}{a_i^v}. \tag{29}$$

Once the pressure–velocity coupling is established and the pressure field is obtained, one must solve the discretized momentum equations

$$\begin{aligned} a_i^u u_i^{n+1} + \sum_{k=1}^{4} a_k^u u_k^{n+1} &= a_i^0 u_i^n - \left(\frac{\partial P}{\partial x} \right)_i r_i A_i + d_i^u, \\ a_i^v v_i^{n+1} + \sum_{k=1}^{4} a_k^v v_k^{n+1} &= a_i^0 v_i^n - \left(\frac{\partial P}{\partial y} \right)_i r_i A_i + d_i^v. \end{aligned} \tag{30}$$

It is noted that in (30) the discretization of the pressure gradient is not yet determined. One can approximate the pressure gradient components by projecting the pressure difference ΔP in directions x and y as done in (26). However, this approach shows some limitations that will now be discussed.

Pressure reconstruction: different approaches

Method 1

In order to solve the momentum equations for u and v, one must first determine the pressure gradients in directions x and y. The most straightforward way to do this is to simply consider these as being equal to the pressure terms in (26) (Method 1):

$$(\partial P/\partial x)_i A_i r_i \approx \Delta P_i N_{ix} s_i r_i, \tag{31}$$

$$(\partial P/\partial y)_i A_i r_i \approx \Delta P_i N_{iy} s_i r_i. \tag{32}$$

Strictly speaking, this is a pressure difference, not a gradient. In fact, it may be considered as the projection of the pressure gradient in the direction normal to the side. This is inadequate, because the computation of a gradient requires at least three points. For quadrilateral staggered grids the

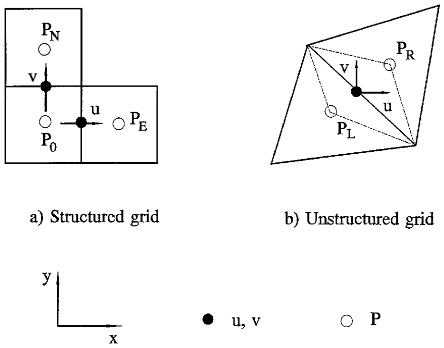

a) Structured grid

b) Unstructured grid

Figure 5. Unstructured and structured staggered grid configurations

configuration of the variables satisfies this condition (Figure 5(a)). Unfortunately, this is not the case for triangular unstructured staggered grids, where both velocity components use the same control volume (Figure 5(b)) and are thus connected to only two pressure points, P_R and P_L. It follows that the pressure difference $\Delta P_i = P_R - P_L$ in (31) and (32) cannot correct both u and v, but only the velocity component normal to a side. This shortcoming stems from the fact that the velocity components are collocated at the sides. This problem will not arise if the velocity components are collocated at the vertices, but then the checkerboard pressure problem appears.[11]

To alleviate the difficulty encountered with Method 1, one may reconstruct the pressure field surrounding an element using as many of the neighbouring pressure points as are necessary to determine the correct pressure gradient. Three alternatives are considered.

At this point a question may arise concerning the use of the pressure difference ΔP in the pressure–velocity coupling step (26) even though this approach does not adequately approximate the pressure gradient in (30). The reason for using ΔP in this manner arises from the fact that equation (26) is derived using ΔP and then coupled to the discretized continuity equation (27) to replace the *normal velocity* to the side. Hence, as far as the normal velocity is concerned, the pressure difference ΔP is the appropriate approximation of the pressure gradient to be used. However, for the momentum equations (30), both u and v must be provided with the correct pressure gradient and thus resorting to a pressure reconstruction may be justified.

This process may in some way be compared to the predictor–corrector method where ΔP is first used to get the correct pressure field and then a pressure reconstruction follows to give the correct velocity components.

To pursue this point further, the present scheme was applied using a coupled version where all the equations are gathered in the same linearized system (u, v, p). The pressure then appears only in the momentum equations and only one pressure gradient discretization is possible. The results show that the approximation with ΔP yields acceptable results as long as the mesh is not very stretched and the flow is not subject to large recirculating regions. Moreover, with the exception of the ΔP approximation, all the pressure reconstructions methods fail to yield adequate predictions. This fact confirms that for the SIMPLER-type algorithm the use of ΔP in the pressure–velocity coupling step is necessary in order to drive the solution to the right results.

Method 2

The most obvious alternative to Method 1 is to assume that the local pressure field varies linearly over macroelement $P_1P_2P_3$ described by the chain lines in Figure 4. The partial derivatives $\partial P/\partial x$ and

$\partial P/\partial y$ needed for the momentum equations are computed from a linear interpolation function uniquely determined from the values of the pressure at points P_1, P_2 and P_3 and their corresponding locations.

Method 3

Unfortunately, Method 2 does not take into consideration the pressure P_0 of the element in question. This value may nevertheless be included in the calculation by computing three pressure gradients for each element via three distinct linear interpolations that will involve P_0 and two other pressure points among P_1, P_2 and P_3. For example, the pressure gradient around vertex 1 is computed using P_0, P_1 and P_2, so the three linear pressure fields covering the element will have P_0 as an intersection point (Figure 6). Hence each velocity control volume intersects with two pressure gradient fields within an element.

Method 4

Although both of the last two alternatives yield acceptable results for the flow field, neither allows the local mass conservation criteria to be satisfied to machine accuracy as is the case for Method 1. This behaviour is due to the slight inconsistency between the pressure differential ΔP_i used in the pressure–velocity coupling equation (28) and the pressure gradients $\partial P/\partial x$ and $\partial P/\partial y$ obtained by either reconstruction Method 2 or Method 3. In order for mass to be strictly conserved, the local pressure field reconstruction must ensure that the normal pressure gradient component $\Delta P_i s_i r_i$ at side i is the same for both equation (28) and the pressure reconstruction, i.e.

$$\Delta P_i s_i r_i = \left[\left(\frac{\partial P}{\partial x}\right) N_{ix} + \left(\frac{\partial P}{\partial y}\right) N_{iy}\right] A_i \bar{r}_{A_i}. \tag{33}$$

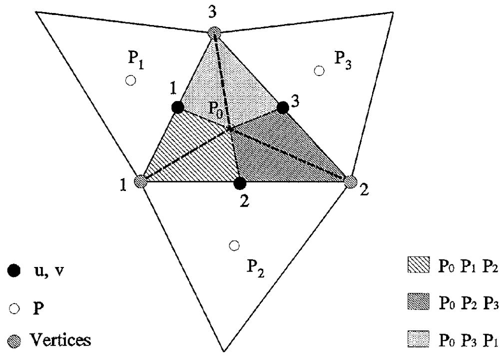

Figure 6. Method 3: pressure reconstruction involving P_0

This may be achieved by deriving a linear interpolation for the pressure that is subject to the constraint described in (33). The following set of equations is then obtained (this example is for side 1 and similar equations are obtained for the other sides (Figure 4)):

$$\begin{aligned} \alpha_1 N_{1x} + \beta_1 N_{1y} &= \Delta P_1 r_1 s_1/(A_1 \bar{r}_{A_1}), \\ \alpha_1 x_2 + \beta_1 y_2 + \gamma_1 &= P_2, \\ \alpha_1 x_3 + \beta_1 y_3 + \gamma_1 &= P_3, \end{aligned} \tag{34}$$

where α_1, β_1 and γ_1 are the coefficients of the linear interpolation around side 1.

This third alternative uses three distinct linear variations of the pressure field within an element and provides a link between the pressure equation (28) and the pressure distribution by ensuring, through the reconstruction, that the normal pressure gradient is continuous across the side.

Finally, for a given pressure reconstruction method the following discretized momentum equations are solved to obtain the velocity field:

$$\begin{aligned} a_i^u u_i^{n+1} + \sum_{k=1}^{4} a_k^u u_k^{n+1} &= a_i^0 u_i^n - \alpha_i r_i A_i + d_i^u, \\ a_i^v v_i^{n+1} + \sum_{k=1}^{4} a_k^v v_k^{n+1} &= a_i^0 v_i^n - \beta_i r_i A_i + d_i^v, \end{aligned} \tag{35}$$

where α_i and β_i are either constant by element (Method 2), a combination of the vertex-based pressure gradients (Method 3) or constant by velocity control volume within an element (Method 4).

Boundary conditions

For the side-centred scheme the boundary control volume has two internal faces and a boundary side (Figure 7), which reduces to two the number of neighbours of calculation point *i*. The discretized equation of a dependent variable ϕ can be then deduced from (16) by adding the contribution of boundary side *i* as follows:

$$a_i \phi_i^{n+1} + \sum_{k=1}^{2} a_k \phi_k^{n+1} + \dot{m}_i \phi_i^{n+1} - q_i = a_i^0 \phi_i^n + d_i^{\phi}, \tag{36}$$

where $\dot{m}_t$ is the mass flow and q_i is the diffusion flux leaving the domain through side *i*. For a Dirichlet-type boundary condition, equation (36) can be replaced by $\phi_i = \phi_{\text{specified}}$ or, if needed,

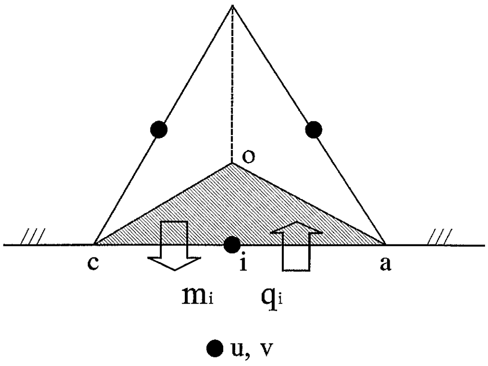

Figure 7. Boundary computational point

solved with q_i as unknown. Otherwise, for Neumann-type boundary conditions, ϕ_i is obtained by solving equation (36).

SOLUTION OF DISCRETIZED EQUATIONS

The solution procedure is based on a SIMPLER-type algorithm in which a pressure correction P' is added to the velocity field to satisfy the continuity equation.[12] The pressure correction should be determined using the same pressure field reconstruction technique as that used to determine the pressure gradient terms $\partial P/\partial x$ and $\partial P/\partial y$. However, reconstructing P' cannot guarantee that the corrected velocity field will satisfy the continuity equation. In fact, for the SIMPLER algorithm, in order for the corrected velocity field to satisfy continuity, P' must satisfy the equation

$$c_0 P'_0 + \sum_{i=1}^{3} c_i P'_i = \xi', \qquad (37)$$

with

$$\xi' = \sum_{i=1}^{3} \rho r_i s_i (\vec{v}_i \cdot \vec{n}_i).$$

Therefore, since satisfying continuity to machine accuracy places a constraint on P', any reconstruction of this pressure correction will result in a certain numerical error. Moreover, as pointed out by Prakash and Patankar,[14] the use of the pressure correction to correct the velocities can be viewed as an artifice to accelerate the convergence. In fact, at convergence the pressure correction is zero. Therefore the pressure correction step has been omitted from the algorithm. The overall procedure can be outlined as follows.

1. Estimate values for all the dependent variables involved.
2. Compute the pseudovelocities u^* and v^* (equation (29)).
3. Solve the pressure equation (28) implicitly over the entire field.
4. Compute the new pressure gradient field using one of the pressure reconstruction methods.
5. Solve the momentum equations (35) implicitly.
6. Solve any additional transport equation as the case may be (equation (16)).
7. Check for convergence of all the variables and return to step 2 after updating the variables unless the convergence criterion has been reached.

Since this algorithm will not necessarily allow continuity to be satisfied to machine accuracy, one may consider another velocity field ($\tilde{u}$, $\tilde{v}$), called the *convecting velocity* field. This is introduced in the spirit of the equal-order methods of Prakash and Patankar[14] as follows:

$$\tilde{u}_i = u_i - \Delta P'_i s_i r_i N_{ix}/a^u_i, \qquad \tilde{v}_i = v_i - \Delta P'_i s_i r_i N_{iy}/a^v_i. \qquad (38)$$

Since using the pressure correction P' in this manner does not involve a reconstruction technique, the so-called convecting velocity field will then satisfy the continuity equation as pointed out earlier. Hence, in every convection–diffusion equation, $\tilde{u}$ and $\tilde{v}$ are the components used as convecting velocities, whereas u and v remain the convected velocity components. The following steps are then added to the overall procedure.

5(a). Solve the pressure correction equation (37) implicitly.
5(b). Compute the convecting velocity field (equation (38)).

NUMERICAL RESULTS

The proposed scheme was validated by comparison with analytical or experimental data from the literature for the following test cases: (i) cavity flow driven by shear and body forces; (ii) backward-facing step flow; (iii) flow over a two-dimensional obstacle; (iv) flow in a pipe with sudden contraction of cross-sectional area.

In this study, only steady state solutions are presented. Computations were carried out on an IBM RISC 6000 model 340. The convergence of a dependent variable ϕ is considered to be reached when both the correction C_ϕ and the residual Res_ϕ tend to zero:

$$C_\phi = \max_{i=1}^{N} |\phi_i^{n+1} - \phi_i^n|, \tag{39}$$

$$Res_\phi = \left[\sum_{i=1}^{N}\left(a_i\phi_i^{n+1} + \sum_{k=1}^{4} a_k\phi_k^{n+1} - a_i^0\phi_i^n - d_i^\phi\right)\right]^{1/2}, \tag{40}$$

where N is the number of computational points in the domain.

Cavity flow driven by shear and body forces

In order to assess the accuracy of the method and to establish the order of the scheme, a grid convergence study is carried out on a benchmark problem with a known analytical solution. The test is a two-dimensional cavity flow driven by shear and body forces (Figure 8). For this test the governing equations for incompressible flows are given by

$$\frac{\partial u}{\partial x} + \frac{\partial v}{\partial y} = 0, \tag{41}$$

$$\frac{\partial}{\partial x}(\rho uu) + \frac{\partial}{\partial y}(\rho uv) - \frac{\partial}{\partial x}\left(\mu\frac{\partial u}{\partial x}\right) - \frac{\partial}{\partial y}\left(\mu\frac{\partial u}{\partial y}\right) + \frac{\partial P}{\partial x} = 0, \tag{42}$$

$$\frac{\partial}{\partial x}(\rho uv) + \frac{\partial}{\partial y}(\rho vv) - \frac{\partial}{\partial x}\left(\mu\frac{\partial v}{\partial x}\right) - \frac{\partial}{\partial y}\left(\mu\frac{\partial v}{\partial y}\right) + \frac{\partial P}{\partial y} - B(x, y, \mu) = 0, \tag{43}$$

where $B(x, y, \mu)$ is a forcing term prescribed as[5]

$$B(x, y, \mu) = -8\mu[24F(x) + 2f'(x)g''(y) + f'''(x)g(y)] - 64[F_2(x)G_1)(y) - g(y)g'(y)F_1(x)] \tag{44}$$

and the functions appearing in (44) are defined as

$$\begin{aligned} f(x) &= x^4 - 2x^3 + x^2, & g(y) &= y^4 - y^2, \\ F(x) &= \int_0^x f(z)\,\mathrm{d}z, & F_1(x) &= f(x)f''(x) - [f'(x)]^2, \\ F_2(x) &= 0{\cdot}5[f(x)]^2, & G_1(y) &= g(y)g'''(y) - g'(y)g''(y). \end{aligned} \tag{45}$$

The boundary conditions are of the Dirichlet type for both u and v, which makes the solution unique for the velocity field. Furthermore, the singularity usually encountered at the top corners in a regular driven cavity flow is eliminated by setting the top boundary velocity to[5]

$$u(x, 1) = 16(x^4 - 2x^3 + x^2). \tag{46}$$

The exact solution to this problem is determined as

$$u(x, y) = 8f(x)g'(y), \qquad v(x, y) = -8f'(x)g(y), \tag{47}$$

$$P(x, y, \mu) = 8\mu[F(x)g'''(y) + f'(x)g'(y)] + 64F_2(x)[g(y)g''(y) - (g'(y))^2], \tag{48}$$

where the pressure depends solely on the Reynolds number.

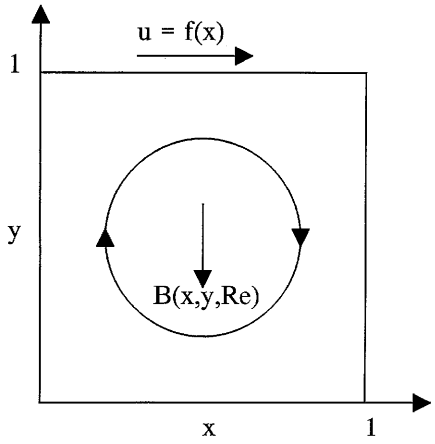

Figure 8. Global features of flow pattern for driven cavity

In order to establish the order of the scheme, seven test cases are carried out at $Re = 10$ where the only parameter allowed to vary is the grid resolution over the domain Ω. The computations are deemed converged when the residual and the corrections of all the dependent variables are less than 10^{-10}. The measure of accuracy is based on the following numerical errors over domain Ω:

$$E_u = \|u - u^{\text{exact}}\|_{1,\Omega}, \qquad E_v = \|v - v^{\text{exact}}\|_{1,\Omega}, \qquad E_{\tilde{P}} = \|\tilde{P} - \tilde{P}^{\text{exact}}\|_{0,\Omega}, \tag{49}$$

where the above L_2 and H_1 norms are defined over a domain Ω for a dependent variable ϕ by

$$\|\phi\|_{0,\Omega} = \left(\int_\Omega |\phi|^2 \,\mathrm{d}\Omega\right)^{1/2}, \qquad \|\phi\|_{1,\Omega} = \|\phi\|_{0,\Omega} + \left[\int_\Omega \left(\left|\frac{\partial\phi}{\partial x}\right|^2 + \left|\frac{\partial\phi}{\partial y}\right|^2\right) \mathrm{d}\Omega\right]^{1/2} \tag{50}$$

and the normalized pressure $\tilde{P}$ is defined by

$$\tilde{P} = P - P^{\text{ref}}, \qquad P^{\text{ref}} = \frac{\int_\Omega P \,\mathrm{d}\Omega}{\int_\Omega \mathrm{d}\Omega}. \tag{51}$$

For this problem the pressure reconstruction methods were first tested without using steps 5(a) and 5(b) in the overall solution procedure. The order of the scheme can be determined by computing the slope of the curves representing the evolution of the true error for the velocity and the pressure fields (Figure 9). In all cases this value is found to be one. Nevertheless, the most appropriate norm to be considered is the L_2 norm for both fields. In fact, for this scheme, neither the velocity nor the pressure is continuous over the domain. Therefore any reference to the H_1 norm to determine the order of the scheme is erroneous.

Methods 1, 2 and 3 seem to behave adequately in spite of their previously discussed drawbacks. However, Method 4, which was introduced in order to satisfy local mass conservation to machine accuracy, strongly affects the pressure field (Figure 9). Moreover, for all the methods the pressure difference $P_{\max} - P_{\min}$ was computed for the finest grid (70 × 70) and compared with its exact value: one can clearly notice that Method 4 yields an incorrect pressure field and should be definitively discarded (Table I).

The problem of mass conservation can be resolved by modifying the algorithm and introducing a so-called convecting velocity $(\tilde{u}, \tilde{v})$ which takes into account the mass conservation through a pressure correction P'. As shown in steps 5(a) and 5(b), this modification to Method 2 yields the best

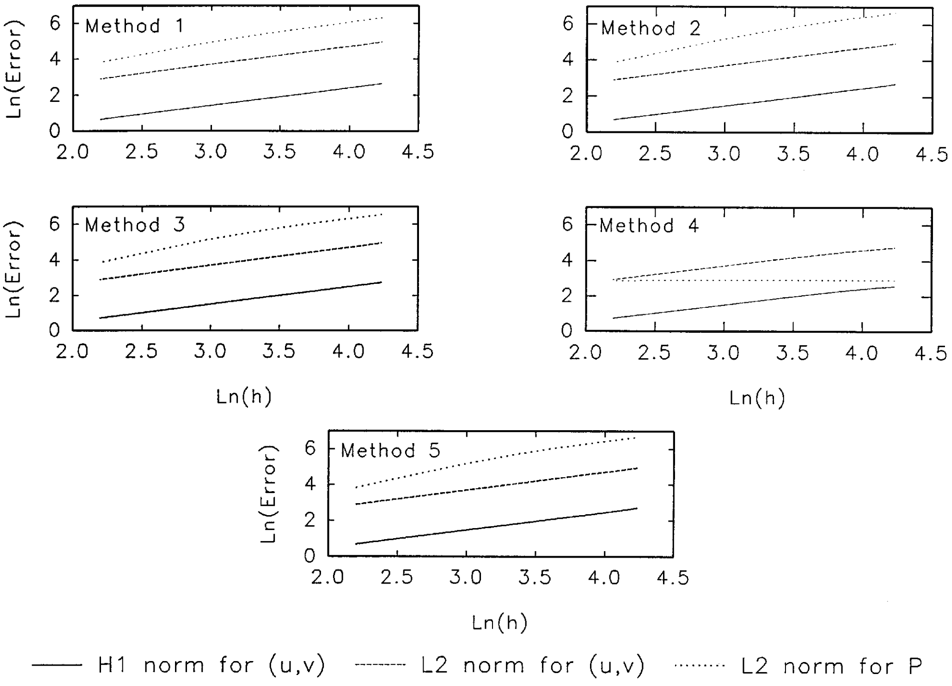

Figure 9. Evolution of true error with cell dimension h

combination (Method 5) and allows both mass conservation and pressure gradient approximation criteria to be satisfied (Figure 9). All the following validations were carried out using this last combination.

Backward-facing step flow

The problem is summarized in Figure 10. A parabolic velocity profile deduced from the experimental measurements of Armaly *et al.*[15] is imposed at the inlet. The computational domain is limited to the region downstream of the expansion. The Reynolds number, based on twice the inlet height and on the average inlet velocity, is equal to 389.

The computational grid contains 3436 sides and 2240 elements. It is fine in the inlet region and stretched near the outlet. Convergence was reached in 1197 s. Predictions for the velocity component u are compared with the experimental data of Reference 15 at the four axial stations $x/S=2{\cdot}55$, 4·18, 7·76 and 13·57.

The present scheme provides very good agreement between numerical computations and experimental data, even at station $x/S=7{\cdot}76$ located near the reattachment point (Figure 11). This agreement is confirmed by the computed recirculation length ($x/S=7{\cdot}65$), which is very close to the experimental value ($x/S=7{\cdot}81$).

Table I. Maximum pressure difference in driven cavity

Method	1	2	3	4	5	Exact
$P_{\max} - P_{\min}$	0·7839	0·7871	0·7855	0·5406	0·7872	0·8249

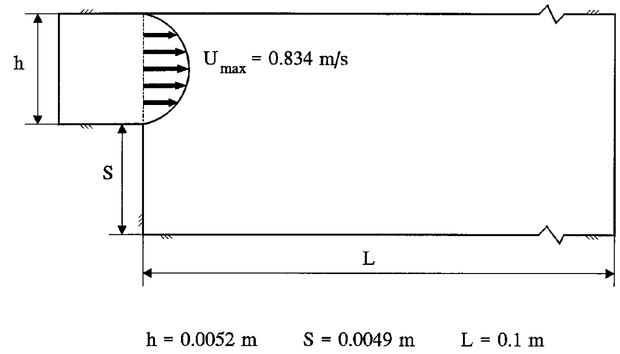

Figure 10. Global features of backward-facing step flow

Laminar flow over a two-dimensional obstacle

The experimental configuration is presented in Figure 12. The velocity profile imposed at the inlet is deduced from the experimental investigations of Carvalho *et al.*[16] The Reynolds number (based on the obstacle height and on the average inlet velocity) is equal to 145. A mesh containing 5766 sides and 3760 elements is used for this computation. The grid is fine around the obstacle and stretched near the outlet. Convergence was reached in 4796 s, which gives a clue about the severity of the test. Figure 13 shows the radial distribution of the velocity component u at eight stations downstream of the obstacle: $x/S = 0$, 2·4, 3·4, 4·4, 6, 11, 18 and 24.

The numerical results are in good agreement with the experimental data. Despite the difficulty of the test, a good recirculation length has been computed ($x/S = 9{\cdot}23$) which is close to the experimental reattachment point obtained by Carvalho *et al.*[16] ($9 < x/S < 11$). A slight difference can be noticed between computed and measured values of the velocities at station $x/S = 11$, which is quite understandable since this station is located at the end of the vortex region.

Laminar flow in a pipe with sudden contraction

This test was experimentally investigated by Durst and Loy.[17] It was selected in order to validate the scheme for axisymmetric flow simulations. The geometric and flow characteristics are given in

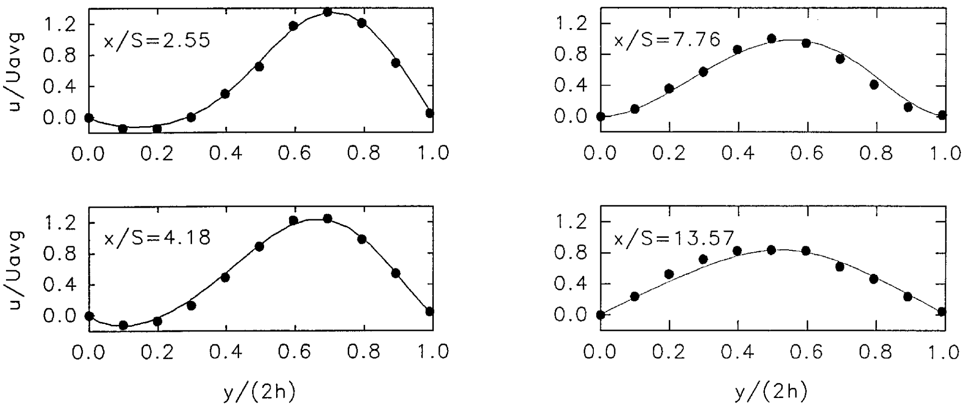

Figure 11. Comparison of measured[15] and predicted u-velocity at various locations of backward-facing step flow

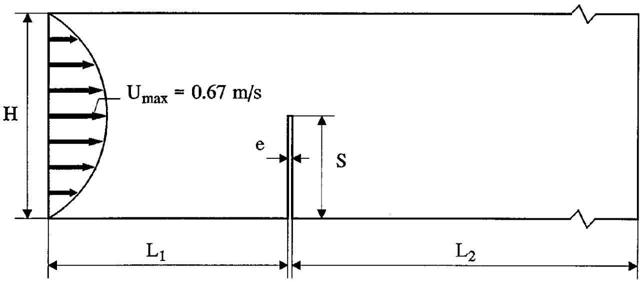

S = 0.005 m e = 0.001 m H = 0.010 m

L_1 = 0.030 m L_2 = 0.120 m

Figure 12. Global features of flow over two-dimensional obstacle

Figure 14. The inlet parabolic profile is deduced from the experimental measurements. The Reynolds number based on the average inlet velocity and on the inlet diameter is equal to 196. The axial velocity profiles both upstream and downstream of the contraction were used for comparison with experimental data at $x/D = -1{\cdot}047$, $-0{\cdot}209$, $-0{\cdot}039$, $0{\cdot}052$, $0{\cdot}105$ and $1{\cdot}000$.

The computational domain is only half the geometric domain because of the axisymmetric nature of the problem. The grid used is unstructured and contains 2537 sides and 1655 elements (Figure 15). The programme converged in 184 s.

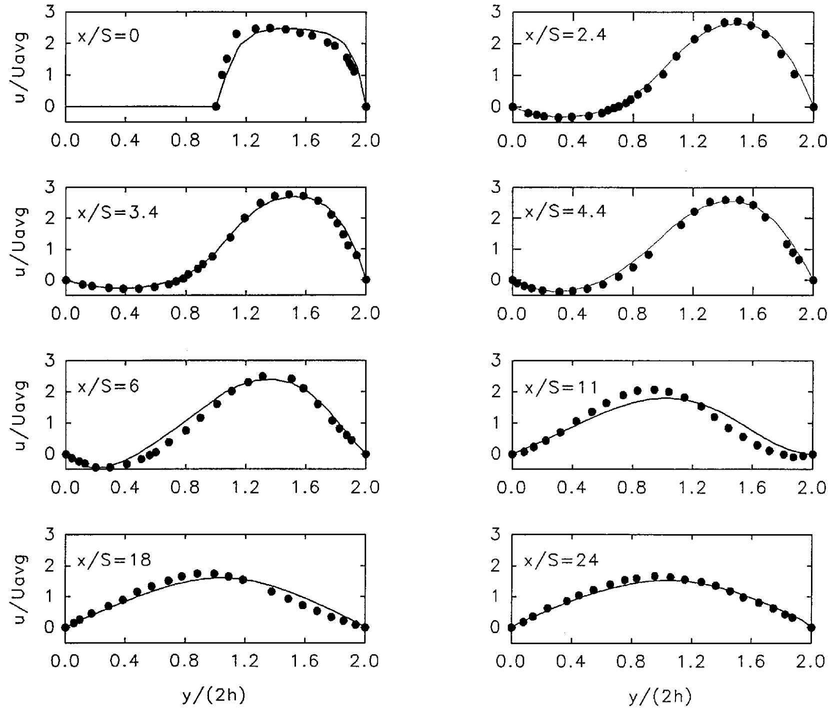

Figure 13. Comparison of measured[16] and predicted u-velocity at various locations for flow over two-dimensional obstacle

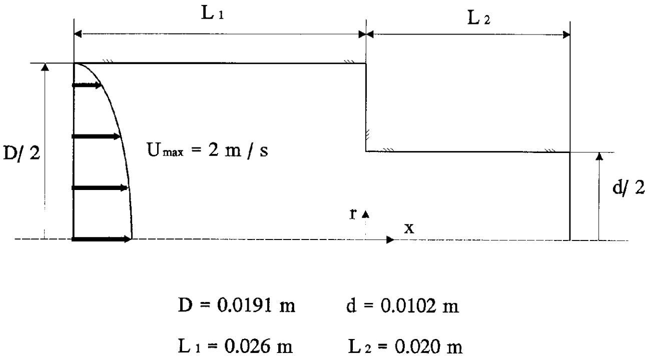

Figure 14. Global features of sudden contraction flow in pipe

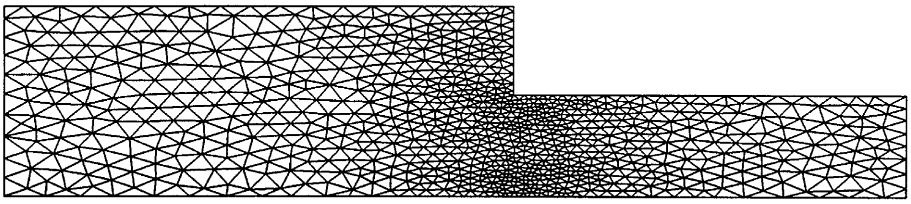

Figure 15. Mesh for pipe with sudden contraction

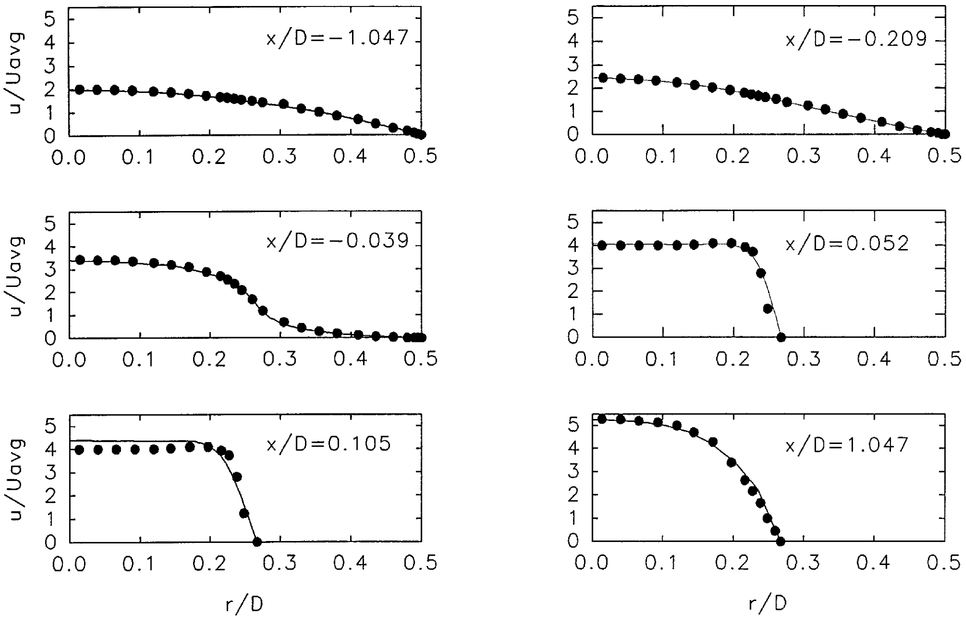

Figure 16. Comparison of measured[17] and predicted axial velocity at various locations for flow in pipe with sudden coantraction

The agreeement, as shown in Figure 16, is very good even in the area of the contraction, confirming both the accuracy of the scheme and its ability to adequately simulate laminar flows.

CONCLUDING REMARKS

An unequal-order staggered control volume method for the prediction of two-dimensional incompressible fluid flow has been presented. The idea of using unstructured staggered grids first emerged with Nicolaides' approach to discretizing the so-called div–curl equations and the Navier–Stokes equations.[18] It consists of using pairs of control volumes that are orthogonally related via a Voronoi–Delaunay triangulation. One set of covolumes holds the circulation of the velocity field and the other is associated with the mass flux. The Navier–Stokes equations are therefore expressed in terms of divergence and curl.

However, in order to avoid the stretching limitations imposed by the Voronoi–Delaunay meshes, the orthogonality property between the two sets of covolumes was eliminated. Furthermore, the two staggered covolumes used in this study were associated with the velocity and the pressure instead of the divergence and the curl. The scheme is not subject to boundary condition problems like the equal-order formulation or the vorticity–streamfunction formulation. It also uses a continuity-satisfying field ($\tilde{u}$, $\tilde{v}$) as the convecting velocity field in all the convection–diffusion equations (including u and v) to strictly ensure mass conservation. Nevertheless, a problem arises concerning the discretization of the pressure gradient when it comes to solving the momentum equations. To alleviate this difficulty, four reconstruction methods of the pressure field are tested, but only one of these (Method 2) yields satisfactory results when combined with the convecting velocity.

The numerical predictions obtained for two-dimensional laminar planar and axisymmetric flows show very good agreement with experimental data. This study also represents a prelude to the numerical solution of turbulent cold flows and turbulent reacting flows using the staggered grid methodology and a large step towards the solution of three-dimensional problems on unstructured tetrahedral meshes.

ACKNOWLEDGEMENTS

The authors wish to aknowledge the support of the National Sciences and Engineering Research Council of Canada (NSERC), FCAR and Centre des Technologies du Gaz Naturel (CTGN) which made the work leading to this study possible.

REFERENCES

1. A. J. Chorin, 'A numerical method for solving incompressible viscous flow problems', *J. Comput. Phys.*, **2**, 12 (1967).
2. B. Koren, 'Improving Euler computations at low Mach numbers', *Proc. Int. Workshop on Solution Techniques for Large-Scale CFD Problems*, Montreal, September 1994, pp. 333–357.
3. C. L. Merkle and M. Athavale, 'Time-accurate unsteady incompressible flow algorithms based on artificial compressibility', *AIAA Paper 87- 1137*, 1987.
4. F. H. Harlow and J. E. Welch, 'Numerical calculation of time- dependent viscous incompressible flow of fluid with free surface', *Phys. Fluids*, **8**, 2182–2189 (1965).
5. T. M. Shih, C. H. Tan and B. C. Hwang, 'Effects of grid staggering on numerical schemes', *Int. j. numer. methods fluids*, **9**, 193– 212 (1989).
6. G. E. Schneider and M. J. Raw, 'Control volume finite-element method for heat transfer and fluid flow using collocated variables—1. Computational procedure', *Numer. Heat Transfer*, **11**, 363–390 (1987).
7. C. M. Rhie and W. L. Chow, 'A numerical study of the turbulent flow past an isolated aerofoil with trailing edge separation', *AIAA Paper 82-0998*, 1982.
8. R. A. Nicolaides, 'The covolume approach to computing incompressible flows', in *Incompressible Computational Fluid Dynamics*, Cambridge University Press, Cambridge, 1993, pp. 295–333.

9. G. E. Schneider and M. J. Raw, ‘A skewed positive influence coefficient procedure for control-volume-based finite-element convection–diffusion computation’, *Numer. Heat Transfer*, **9**, 1–26 (1986).
10. B. R. Baliga and S. V. Patankar, ‘A new finite-element formulation for convection–diffusion problems’, *Numer. Heat Transfer*, **3**, 393–409 (1980).
11. S. Rida, ‘Méthode de volumes finis pour la simulation numérique d’écoulements turbulents sur des maillages non-structurés’, *M.Sc.A Thesis*, Department of Mechanical Engineering, École Polytechnique de Montréal, 1993.
12. S. V. Patankar, *Numerical Heat Transfer and Fluid Flow*, Hemisphere, New York, 1980.
13. F. L. Meng, ‘A staggered control volume finite element method for turbulent reacting flows coupled with radiation’, *Ph.D Thesis*, Department of Mechanical Engineering, École Polytechnique de Montréal, 1994.
14. C. Prakash and S. V. Patankar, ‘A control volume-based finite-element method for solving the Navier–Stokes equations using equal-order velocity– pressure interpolation’, *Numer. Heat Trans.*, **8**, 259–280 (1985).
15. B. F. Armaly, F. Durst, J. C. F. Pereira and B. Schonung, ‘Experimental and theoretical investigations of backward-facing step flow’, *J. Fluid Mech.*, **126**, 473–496 (1983).
16. M. G. Carvalho, F. Durst and J. C. F. Pereira, ‘Predictions and measurements of laminar flow over two-dimensional obstacles’, *Appl. Math. Model.*, **11**, 23–34 (1987).
17. F. Durst and T. Loy, ‘Investigations of laminar flow in a pipe with sudden contraction of cross-sectional area’, *Comput. Fluids*, **13**, 15–36 (1985).
18. R. A. Nicolaides, ‘Flow discretization by complementary volume techniques’, *Proc. 9th AIAA CFD Meet.*, Buffalo, NY, June 1989, AIAA, New York, 1989.